
A Search for New Exotic Particles with Jets in Proton-Proton Collisions at the CMS Experiment

Dissertation

zur

**Erlangung der naturwissenschaftlichen Doktorwürde
(Dr. sc. nat.)**

vorgelegt der

Mathematisch-naturwissenschaftlichen Fakultät

der

Universität Zürich

von

Johnny B. Goode

aus

Deutschland

Promotionskommission

Prof. Dr. Ben Kilminster (Vorsitz)

Prof. Dr. Florencia Canelli

Prof. Dr. Nicola Serra

Prof. Dr. Gino Isidori

Zürich, 20...

2 Abstract

3 The Standard Model of particle physics has been very successful. But there are problems. They
4 can be explained by new exotic particles.

5 A search is presented for a new exotic particle. Events with jets are considered. A novel
6 technique is used. The search is based on Run-2 proton-proton collision data at a center-of-mass
7 energy of 13 TeV recorded with the CMS detector corresponding to an integrated luminosity of
8 137.1 fb^{-1} .

9 Upper limits are set on the production cross section of a new exotic particle as a function of
10 mass. Results are compared with theoretical predictions to obtain lower limits on the mass. At
11 95% confidence level, new exotic particles are excluded for masses below X GeV.

¹³ **Acknowledgements**

¹⁴ I want to thank the great people in the UZH group and at CMS Collaboration that have helped
¹⁵ me along the way, and with whom it was a great privilege and pleasure to work on diverse
¹⁶ projects and push the limits of our understanding of Nature.

¹⁷ Special thanks go to my supervisor, Prof. Dr. ...; my supervisor Dr. ...; ...

¹⁸ I would also like to thank my parents and family, for supporting me along my studies.

Contents

| | | |
|----|--|----|
| 20 | 1 Introduction | 1 |
| 21 | 2 The Standard Model | 2 |
| 22 | 2.1 The Standard Model | 2 |
| 23 | 2.1.1 The Standard Model Lagrangian | 2 |
| 24 | 2.1.2 The gauge sector | 2 |
| 25 | 2.1.3 The Yukawa sector | 5 |
| 26 | 2.1.4 CKM matrix | 5 |
| 27 | 2.2 Higgs | 6 |
| 28 | 2.3 The physics of proton-proton collisions | 6 |
| 29 | 3 Beyond the Standard Model | 8 |
| 30 | 4 The CMS Experiment | 10 |
| 31 | 4.1 The Large Hadron Collider | 10 |
| 32 | 4.1.1 Luminosity | 10 |
| 33 | 4.2 The CMS detector | 12 |
| 34 | 4.2.1 Coordinate system | 13 |
| 35 | 4.2.2 The solenoid magnet & flux-return yoke | 13 |
| 36 | 4.2.3 The pixel tracker | 13 |
| 37 | 4.2.4 The silicon strip tracker | 13 |
| 38 | 4.2.5 The electromagnetic calorimeter | 13 |
| 39 | 4.2.6 The hadronic calorimeter | 13 |
| 40 | 4.2.7 The muon system | 13 |
| 41 | 4.2.8 The trigger system | 15 |
| 42 | 5 Object & Event Reconstruction | 16 |
| 43 | 5.1 Principles of particle identification | 16 |
| 44 | 5.2 Particle-flow algorithm | 16 |
| 45 | 5.3 Primary vertex | 16 |
| 46 | 5.4 Electrons | 16 |
| 47 | 5.5 Muons | 16 |
| 48 | 5.6 Hadronically Decayed τ Leptons | 18 |
| 49 | 5.7 Jets | 18 |
| 50 | 5.8 Bottom quark identification | 18 |
| 51 | 5.9 Missing transverse energy | 20 |
| 52 | 6 Data sets & Simulated Samples | 21 |
| 53 | 6.1 Data sets | 21 |
| 54 | 6.2 Event simulation | 21 |

| | | |
|----|---------------------------------------|-----------|
| 55 | 6.3 Backgrounds | 21 |
| 56 | 6.3.1 Simulated backgrounds | 21 |
| 57 | 6.3.2 Cross sections | 24 |
| 58 | 7 Event Selection | 25 |
| 59 | References | 26 |

60 1 Introduction

61 Over the last 100 years, physicists have made large strides in understanding the natural laws
62 that govern the universe as we know it. The Standard Model (SM) of particle physics describes
63 matter and its interactions.

64 In 2012, the discovery of the Higgs boson was announced by the ATLAS and CMS experiments [1–3] at CERN’s LHC. The Higgs was 47 years before that [4, 5]. Despite its many
65 successes, there are both theoretical and experimental reasons that imply the SM is not the final
66 theory of Nature.

67 This dissertation has the following structure: Chapter 2 discusses the SM, after which Chapter
68 3 motivates the search for new hypothetical particles. Chapter 4 describes the LHC accelerator,
69 CMS detector and the data collection. Chapter 5 describes the physics objects that are
70 relevant for this thesis. After these, Chapter 7 discusses the selections.

72 2 The Standard Model

73 This chapter introduces the Standard Model (SM) of particle physics. I left a bit of text with
74 equations, citations, figures, and tables as an example of this template.

75 2.1 The Standard Model

76 A rough timeline of the experimental discovery of particles is given by Fig. 2.1. More detailed
77 historical discussions can be found in Refs. [6–8].

78 With a mass of $m_t \approx 172.8 \text{ GeV}$ [10, p. 32], the top quark is by far the heaviest fermion.

79 The discovery of the Higgs was announced in 2012 [1–3, 11]. A single Higgs boson is the
80 simplest and most minimal solution, although it is possible to achieve SBB with more than one
81 Higgs boson. No evidence of additional Higgs bosons have been found so far [12].

82 2.1.1 The Standard Model Lagrangian

83 The SM is encoded in the *SM Lagrangian density*. The terms of the Lagrangian density can be
84 grouped into three separate *sectors*:

$$\mathcal{L}_{\text{SM}} = \mathcal{L}_{\text{gauge}} + \mathcal{L}_{\text{Higgs}} + \mathcal{L}_{\text{Yukawa}}. \quad (2.1)$$

85 Secondly, the SM is a *gauge theory*: It has an internal symmetry that corresponds to the
86 local $\text{SU}(3)_C \times \text{SU}(2)_L \times \text{U}(1)_Y$ symmetry group. The SM gauge group is spontaneously broken
87 to

$$\text{SU}(3)_C \times \text{SU}(2)_L \times \text{U}(1)_Y \xrightarrow{\text{SSB}} \text{SU}(3)_C \times \text{U}(1)_{\text{EM}} \quad (2.2)$$

88 by the nonzero vev of the Higgs field, where $\text{U}(1)_{\text{EM}}$ is the gauge symmetry group for QED.

89 2.1.2 The gauge sector

The gauge sector can be written as

$$\mathcal{L}_{\text{gauge}} = \sum_f \sum_{\psi_f} \bar{\psi}_f i\gamma^\mu D_\mu \psi_f - \frac{1}{4} G_{\mu\nu}^a G_a^{\mu\nu} - \frac{1}{4} W_{\mu\nu}^i W_i^{\mu\nu} - \frac{1}{4} B^{\mu\nu} B^{\mu\nu}, \quad (2.3)$$

90 in natural units $c = \hbar = 1$ [14], and where $a = 1, \dots, 8$ and $i = 1, 2, 3$. In the first term, matter
91 is given by five fermion fields ψ_f in three generations $f = 1, 2, 3$;

$$Q_L^f = \begin{pmatrix} u_L^f \\ d_L^f \end{pmatrix}, \quad u_R^f, \quad d_R^f, \quad L_L^f = \begin{pmatrix} \nu_L^f \\ e_L^f \end{pmatrix}, \quad e_R^f. \quad (2.4)$$

92 Their Dirac adjoints are given by $\bar{\psi}_f = \psi_f^\dagger \gamma^0$.

93 The covariant derivative

$$D_\mu = \partial_\mu + ig_s t_a G_\mu^a + ig T_i W_\mu^i + ig' \frac{Y}{2} B_\mu \quad (2.5)$$

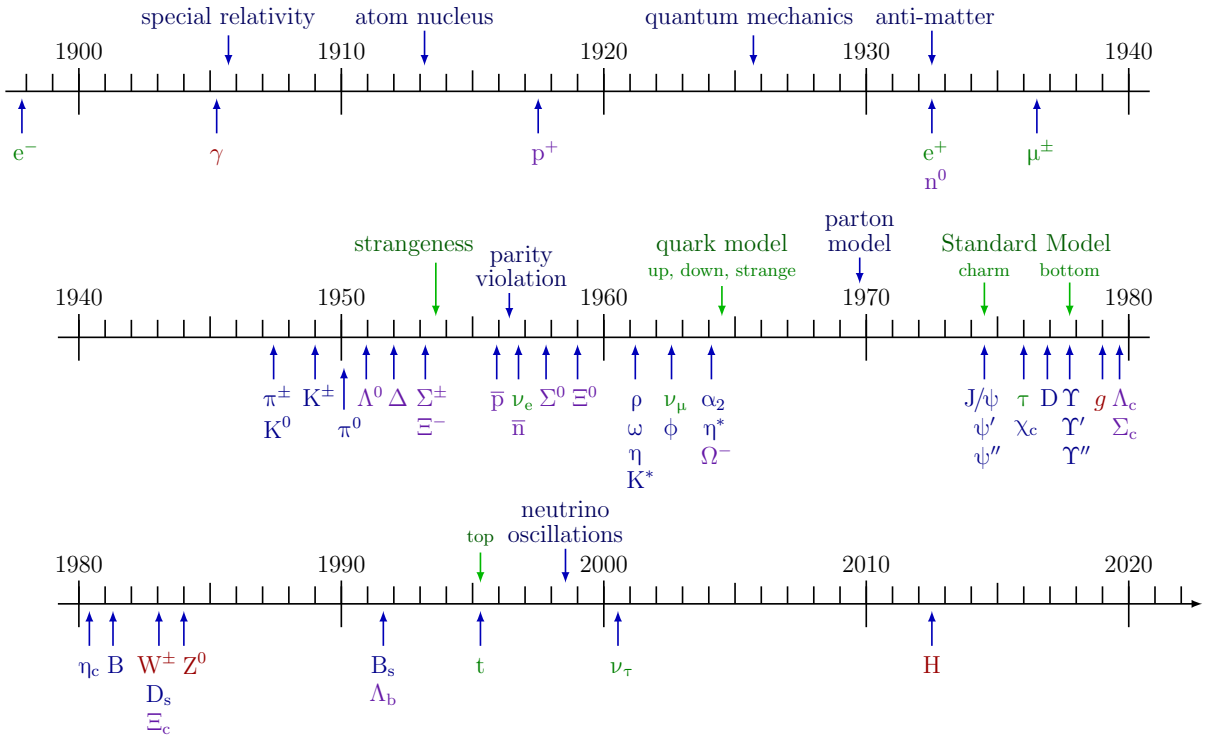


Figure 2.1: A timeline of particle physics in the last 130 years. Adapted from Ref. [9].

| three generations of matter (fermions) | | | interactions / force carriers (bosons) | |
|---|---|---|---|---|
| I | II | III | | |
| mass charge spin | $=2.2 \text{ MeV}/c^2$ $\frac{2}{3}$ $\frac{1}{2}$ u up | $=1.28 \text{ GeV}/c^2$ $\frac{2}{3}$ $\frac{1}{2}$ c charm | $=173.1 \text{ GeV}/c^2$ $\frac{2}{3}$ $\frac{1}{2}$ t top | 0 0 1 g gluon |
| QUARKS | | | | $=124.97 \text{ GeV}/c^2$ 0 0 0 H higgs |
| | $=4.7 \text{ MeV}/c^2$ $-\frac{1}{3}$ $\frac{1}{2}$ d down | $=96 \text{ MeV}/c^2$ $-\frac{1}{3}$ $\frac{1}{2}$ s strange | $=4.18 \text{ GeV}/c^2$ $-\frac{1}{3}$ $\frac{1}{2}$ b bottom | 0 0 1 γ photon |
| LEPTONS | $=0.511 \text{ MeV}/c^2$ -1 $\frac{1}{2}$ e electron | $=105.66 \text{ MeV}/c^2$ -1 $\frac{1}{2}$ μ muon | $=1.7768 \text{ GeV}/c^2$ -1 $\frac{1}{2}$ τ tau | $=91.19 \text{ GeV}/c^2$ 0 0 Z Z boson |
| | $<1.0 \text{ eV}/c^2$ 0 $\frac{1}{2}$ ν_e electron neutrino | $<0.17 \text{ MeV}/c^2$ 0 $\frac{1}{2}$ ν_μ muon neutrino | $<18.2 \text{ MeV}/c^2$ 0 $\frac{1}{2}$ ν_τ tau neutrino | $=80.433 \text{ GeV}/c^2$ ± 1 1 W W boson |
| | | | | GAUGE BOSONS VECTOR BOSONS |

Figure 2.2: A table of the particles in Standard Model of particle physics and their properties. Figure taken from Ref. [13].

Table 2.1: Summary of the representation and quantum numbers SM fields. Bold numbers indicate the dimension of the representation under the respective gauge group.

| Field name | Symbol | Representations | | Quantum numbers | | |
|-------------------------|---|--------------------|--------------------|--|----------------|--|
| | | SU(3) _C | SU(2) _L | T_3 | $Y/2$ | $Q = T_3 + Y/2$ |
| Quark doublet | $Q_L = \begin{pmatrix} u_L \\ d_L \end{pmatrix}$ | 3 | 2 | $\begin{pmatrix} +\frac{1}{2} \\ -\frac{1}{2} \end{pmatrix}$ | $+\frac{1}{6}$ | $\begin{pmatrix} +\frac{2}{3} \\ -\frac{1}{3} \end{pmatrix}$ |
| Up-quark singlet | u_R | 3 | 1 | $+\frac{2}{3}$ | $+\frac{2}{3}$ | $+\frac{2}{3}$ |
| Down-quark singlet | d_R | 3 | 1 | $-\frac{1}{3}$ | $-\frac{1}{3}$ | $-\frac{2}{3}$ |
| Lepton doublet | $L_L = \begin{pmatrix} \nu_L \\ e_L \end{pmatrix}$ | 1 | 2 | $\begin{pmatrix} +\frac{1}{2} \\ -\frac{1}{2} \end{pmatrix}$ | $-\frac{1}{2}$ | $\begin{pmatrix} 0 \\ -1 \end{pmatrix}$ |
| Lepton singlet | e_R | 1 | 1 | 0 | -1 | -1 |
| Gluon field | G_μ^a | 8 | 1 | 0 | 0 | 0 |
| Weak gauge field | $W_\mu^i = \begin{pmatrix} W_\mu^+ \\ W_\mu^- \\ W_\mu^3 \end{pmatrix}$ | 1 | 3 | $\begin{pmatrix} +1 \\ -1 \\ 0 \end{pmatrix}$ | 0 | $\begin{pmatrix} +1 \\ -1 \\ 0 \end{pmatrix}$ |
| Hypercharge field | B_μ | 1 | 1 | 0 | 0 | 0 |
| Higgs doublet | $\Phi = \begin{pmatrix} \phi^+ \\ \phi^0 \end{pmatrix}$ | 1 | 2 | $\begin{pmatrix} +\frac{1}{2} \\ -\frac{1}{2} \end{pmatrix}$ | $+\frac{1}{2}$ | $\begin{pmatrix} +1 \\ 0 \end{pmatrix}$ |
| Conjugate Higgs doublet | $\Phi^c = \begin{pmatrix} \phi^{0*} \\ \phi^- \end{pmatrix}$ | 1 | 2 | $\begin{pmatrix} +\frac{1}{2} \\ -\frac{1}{2} \end{pmatrix}$ | $-\frac{1}{2}$ | $\begin{pmatrix} 0 \\ -1 \end{pmatrix}$ |

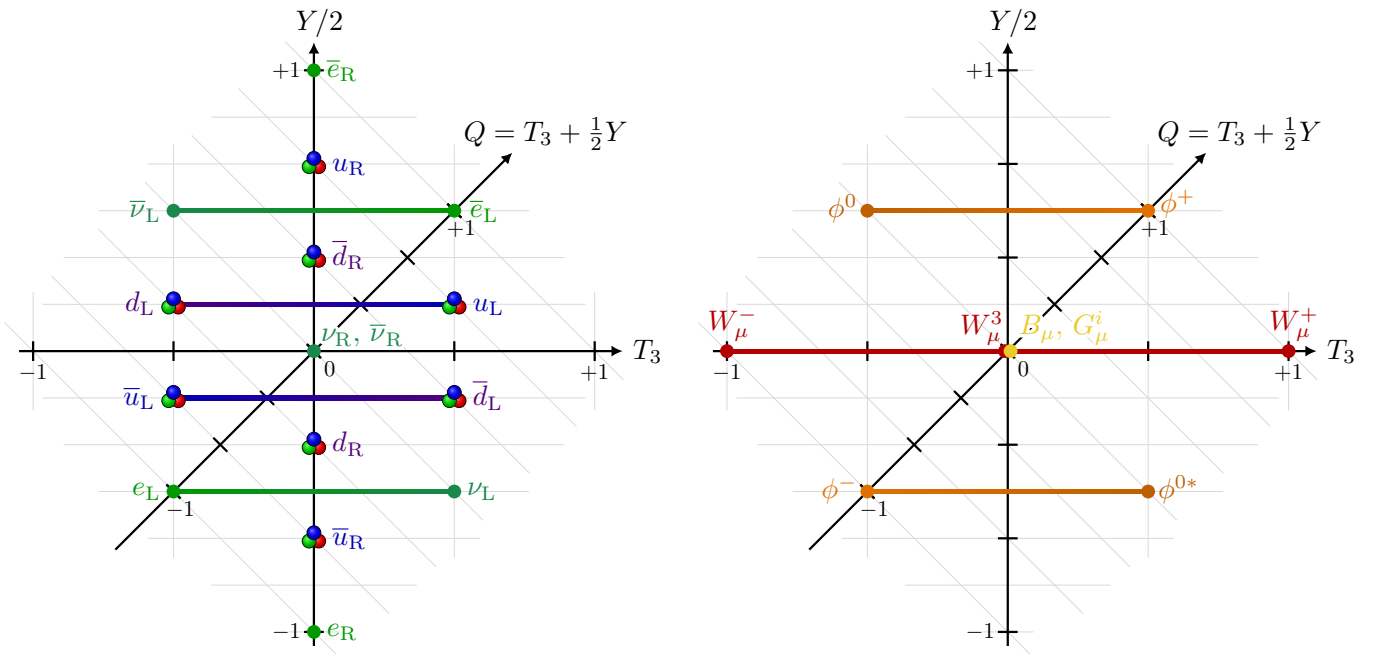


Figure 2.3: Graph of the $(T_3, Y/2)$ quantum numbers.

where T_i and t_a are the generators for $SU(2)_L$ and $SU(3)_C$, respectively, and Y is the weak hypercharge of the field that D_μ acts on.

Through the Higgs mechanism, the gauge bosons acquire mass and mix into the mass eigenstates

$$W_\mu^\pm = \frac{W_\mu^1 \mp iW_\mu^2}{\sqrt{2}}, \quad Z_\mu = W_\mu^3 \cos \theta_W + B_\mu^3 \sin \theta_W, \quad A_\mu = W_\mu^3 \sin \theta_W - B_\mu^3 \cos \theta_W, \quad (2.6)$$

where W_μ^\pm are the charged W boson fields, Z_μ is the neutral Z boson field, A_μ is the photon field, and θ_W is the Weinberg angle given by $\sin \theta_W = g'/\sqrt{g^2 + g'^2}$. After mixing, the new covariant derivative becomes

$$D_\mu = \partial_\mu + ig_s t_a G_\mu^a + i \frac{g}{\sqrt{2}} T^+ W_\mu^+ + i \frac{g}{\sqrt{2}} T^- W_\mu^- + i \frac{g}{\cos \theta_W} (T_3 - \sin^2 \theta_W Q) Z_\mu + ieQ A_\mu, \quad (2.7)$$

with ladder operators $T^\pm = T_1 \pm iT_2$.

2.1.3 The Yukawa sector

In order to explain mass of the fermions,

$$\mathcal{L}_{\text{Yukawa}} = -Y_d^{fg} \bar{Q}_L^f \Phi d_R^g - Y_u^{fg} \bar{Q}_L^f \Phi^c u_R^g - Y_e^{fg} \bar{L}_L^f \Phi e_R^g + \text{h.c.}, \quad (2.8)$$

with the conjugate Higgs doublet $\Phi^c = i\sigma_2 \Phi^\dagger$, and unitary Yukawa matrices Y_d^{fg} , Y_u^{fg} , $Y_e^{fg} \in U(3)$ that mixes the fermion generations. As Φ is a scalar field that forms a weak isospin doublet,

$$\Phi = \begin{pmatrix} \phi^+ \\ \phi^0 \end{pmatrix}. \quad (2.9)$$

Because the Higgs vev is nonzero, we can fix the $SU(2)_L$ gauge. It is convenient to choose the unitary gauge

$$\Phi = \frac{1}{\sqrt{2}} \begin{pmatrix} 0 \\ v + h \end{pmatrix}, \quad (2.10)$$

with the vev $v \approx 246$ GeV, a real constant, and the neutral Higgs field h , a (real) scalar. Therefore, after SSB, we are left with

$$\mathcal{L}_{\text{Yukawa}} = -\frac{Y_d^{fg}}{\sqrt{2}} \bar{d}_L^f (v + h) d_R^g - \frac{Y_u^{fg}}{\sqrt{2}} \bar{u}_L^f (v + h) u_R^g - \frac{Y_e^{fg}}{\sqrt{2}} \bar{e}_L^f (v + h) e_R^g + \text{h.c.} \quad (2.11)$$

2.1.4 CKM matrix

To explain the suppressed decay rate of $K^0 \rightarrow \mu^+ \mu^-$, Glashow, Iliopoulos, and Maiani used a mixing matrix and proposed the existence of the charm quark [15]. This is referred to as the *Glashow–Iliopoulos–Maiani (GIM) mechanism*. The mixing of two quark generations is given by the *Cabibbo matrix*:

$$\begin{pmatrix} d' \\ s' \end{pmatrix} = \begin{pmatrix} \cos \theta_C & \sin \theta_C \\ -\sin \theta_C & \cos \theta_C \end{pmatrix} \begin{pmatrix} d \\ s \end{pmatrix}, \quad (2.12)$$

where $|d'\rangle$ and $|s'\rangle$ represent the weak eigenstates, which are linear combinations of the mass eigenstates $|d\rangle$ and $|s\rangle$. The mixing is quantified with the *Cabibbo angle* $\theta_C \approx 13.04^\circ$.

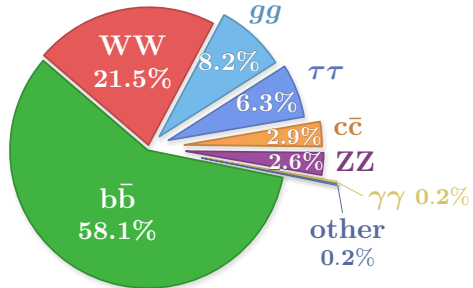


Figure 2.4: Pie chart of Higgs branching fractions.

117 The mixing of three generations is given by

$$\begin{pmatrix} d' \\ s' \\ b' \end{pmatrix} = \begin{pmatrix} V_{ud} & V_{us} & V_{ub} \\ V_{cd} & V_{cs} & V_{cb} \\ V_{td} & V_{ts} & V_{tb} \end{pmatrix} \begin{pmatrix} d \\ s \\ b \end{pmatrix}, \quad (2.13)$$

118 where the matrix is the so-called *Cabbibo-Kobayashi-Maskawa (CKM) matrix*, denoted by V_{CKM} .

119 **2.2 Higgs**

120 A pie chart of Higgs decay can be found in Fig. 2.4.

121 **2.3 The physics of proton-proton collisions**

122 The substructure of the proton has been carefully studied in deep inelastic scattering (DIS)
123 experiments at SLAC [16, 17] and DESY [18], which collided electrons or positrons with protons.

124 In the parton model, *parton distribution functions* (PDFs) describe the probability of finding
125 a parton of type p with momentum fraction x in a collision at some momentum scale Q as a
126 function of the form $f_p(x, Q^2)$ [19–23]. The proton has *valence quarks* and *sea quarks*. To reflect
127 the proton quantum numbers, the PDFs are normalized:

$$\int_0^1 [f_u(x, Q^2) - f_{\bar{u}}(x, Q^2)] dx = 2, \quad \int_0^1 [f_d(x, Q^2) - f_{\bar{d}}(x, Q^2)] dx = 1. \quad (2.14)$$

128 This follows from the factorization theorem [25, 26], which provides a formula to calculate
129 the cross sections of a hard process with an integral of the form

$$\sigma(\text{pp} \rightarrow X + Y) = \sum_{i,j} \int_0^1 \int_0^1 f_i(x_1, Q^2) f_j(x_2, Q^2) \hat{\sigma}_{ij \rightarrow X}(x_1, x_2, Q^2) dx_1 dx_2, \quad (2.15)$$

130 where $\hat{\sigma}_{ij \rightarrow X}(x_1, x_2, Q^2)$ is the parton-level cross section of the hard process, $i + j \rightarrow X$, and
131 parton i (j) carries a fraction x_1 (x_2) of the momentum of its mother proton.

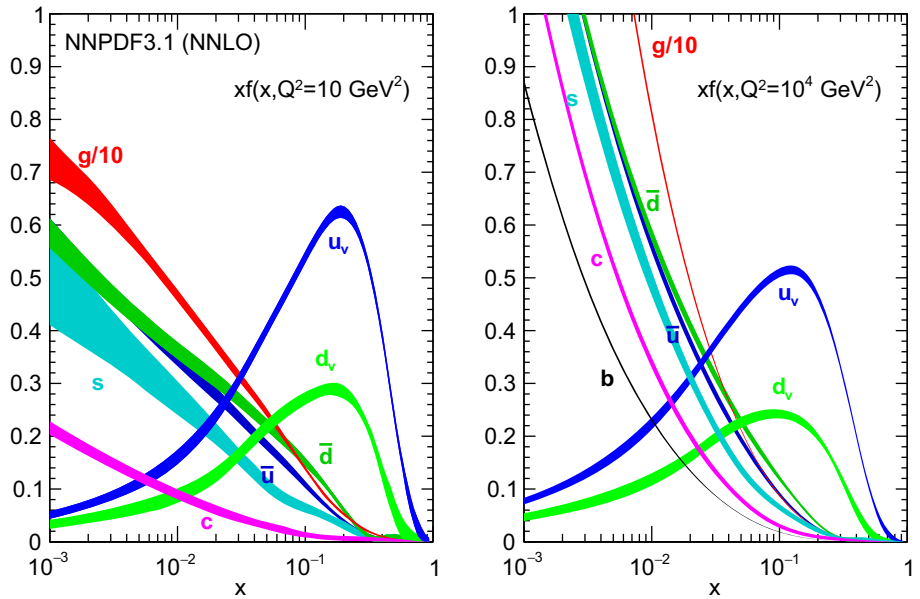


Figure 2.5: Plot of the proton PDF $f_p(x, Q^2)$ times the momentum fraction x as calculated by NNPDF3.1 at NNLO accuracy in perturbation theory for $Q^2 = 10 \text{ GeV}^2$ (left) and $Q^2 = 10^4 \text{ GeV}^2$ (right). Adapted from [24].

¹³² **3 Beyond the Standard Model**

¹³³ The SM of particle physics is successful. Fine-structure constant $\alpha = e^2/4\pi$ has been precisely
¹³⁴ calculated and measured [27–30]. In 2012, the discovery of the Higgs boson was announced by
¹³⁵ the ATLAS and CMS experiments at the CERN LHC [1–3, 11], more than 47 years after its
¹³⁶ prediction [4, 5]. But there are both problems. The following section highlights several examples
¹³⁷ of open questions in physics.

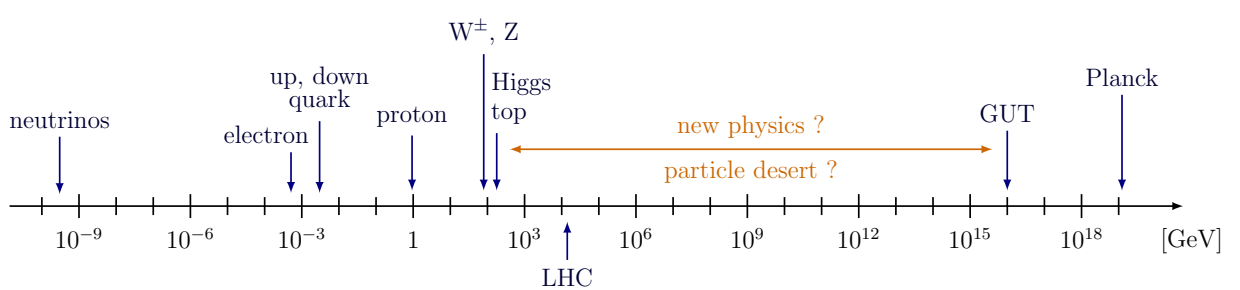


Figure 3.1: Logarithmic scale of different energy scales in particle physics. Adapted from Ref. [9].

¹³⁸ 4 The CMS Experiment

¹³⁹ This chapter will discuss the experimental setup.

¹⁴⁰ 4.1 The Large Hadron Collider

¹⁴¹ The Large Hadron Collider (LHC) is the world's largest and most powerful particle collider
¹⁴² with a 27 km circumference and a record collision energy of 13.6 TeV. It surpasses the Tevatron
¹⁴³ accelerator at Fermilab in the United States [32] (6.3 km, 1.96 TeV), and LEP (209 GeV) [10,
¹⁴⁴ Section 32].

¹⁴⁵ During the data-taking period of 2015 to 2018, referred to as "Run 2", the energy of each
¹⁴⁶ proton beam was 6.5 TeV, which means the center-of-mass energy was $\sqrt{s} = 13$ TeV. The LHC
¹⁴⁷ machine is described in more technical detail in Ref. [33].

¹⁴⁸ 4.1.1 Luminosity

¹⁴⁹ It depends on several beam parameters. The simplified expression is [10, p. 533]:

$$\mathcal{L} = \frac{N_1 N_2 f}{A}. \quad (4.1)$$

¹⁵⁰ The LHC is designed to reach the nominal luminosity of $\mathcal{L} = 10^{34} \text{ cm}^{-2} \text{ s}^{-1}$. See Fig. 4.2. Each
¹⁵¹ bunch contains about 110 billion protons [33, 35].

¹⁵² Figure 4.4 shows the distribution of the number of interactions per bunch crossing in all

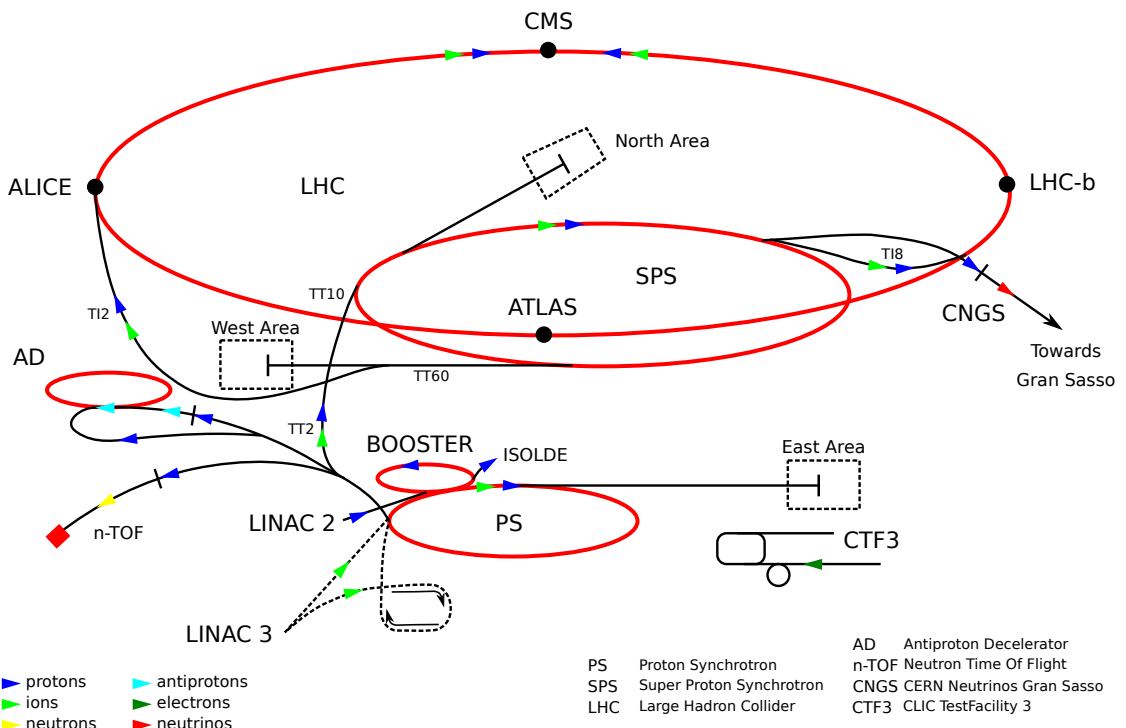


Figure 4.1: CERN's accelerator complex. Taken from [31].

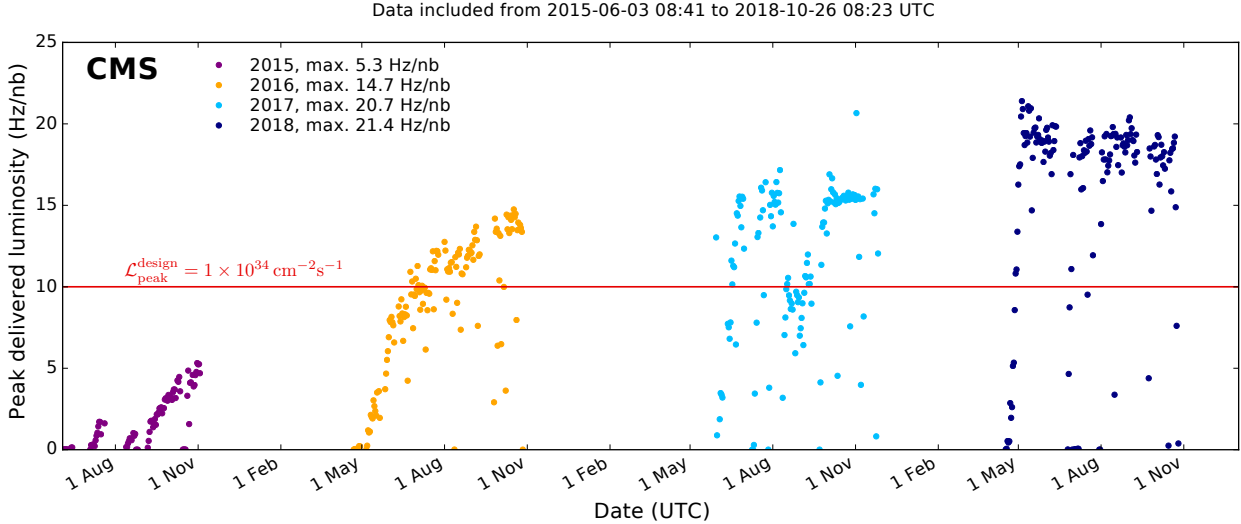


Figure 4.2: The instantaneous luminosity \mathcal{L} . The design luminosity is $\mathcal{L}_{\text{peak}}^{\text{design}} = 10^{34} \text{ cm}^{-2} \text{s}^{-1}$. Adapted from [34].

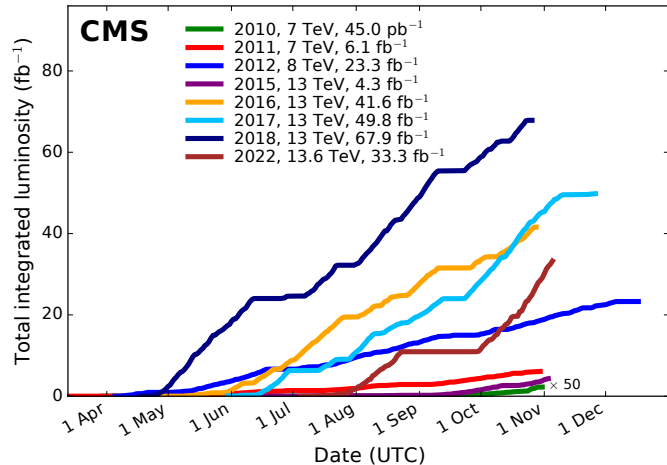


Figure 4.3: Integrated luminosity collected by CMS at $\sqrt{s} = 13 \text{ TeV}$. Figure taken from [34].

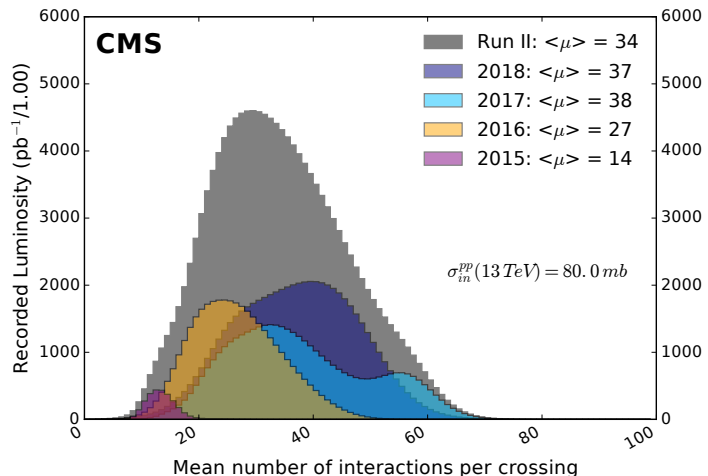


Figure 4.4: Distribution of number of pp interactions, assuming an inelastic cross section of 80 mb. Figure taken from [34].

153 data-taking years of Run 2.

154 Figure 4.3 shows the data of each data-taking year with *integrated luminosity* L , which is

$$L := \int_{\text{data taking}} \mathcal{L}(t) dt, \quad (4.2)$$

155 given in units of inverse area, such as the inverse barn (b^{-1}). Between 2016 and 2018, CMS
156 collected about 138 fb^{-1} of pp collision data for physics analysis.

157 4.2 The CMS detector

158 The Compact Muon Solenoid (CMS) detector at one of the interaction points at the LHC. An
159 illustration is shown in Fig. 4.5. A detailed description can be found in Ref. [36].

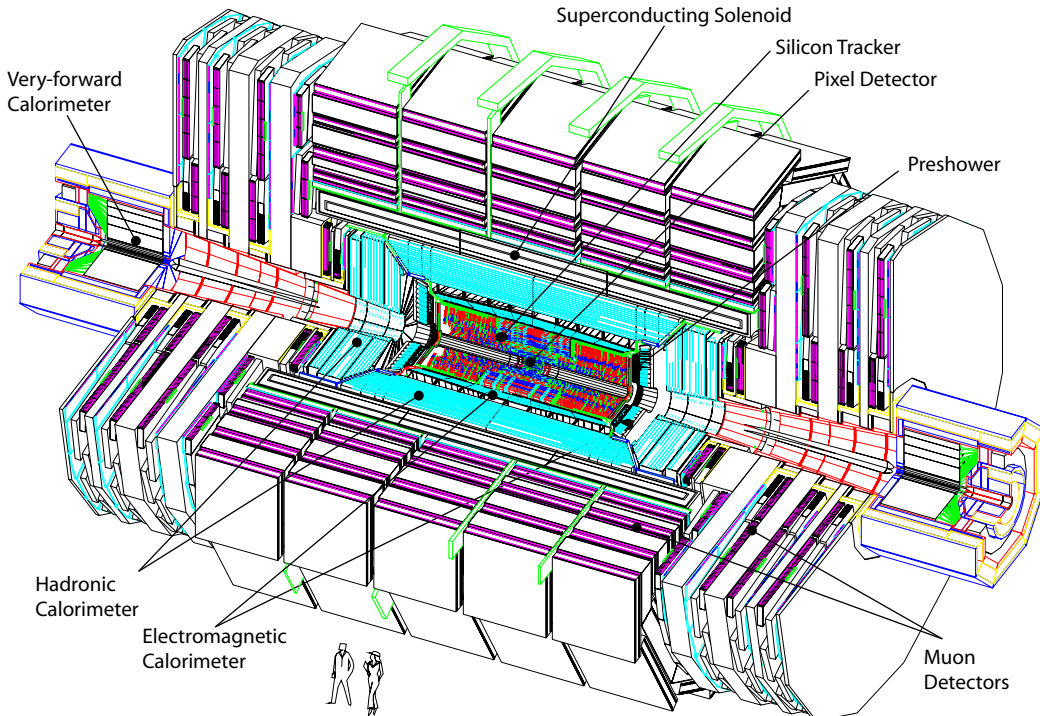


Figure 4.5: The CMS detector. Taken from [36].

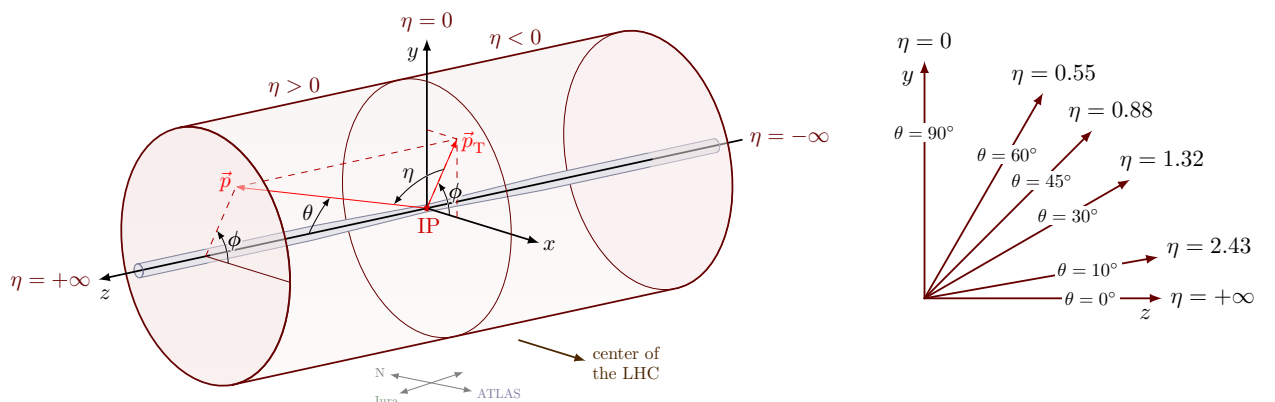


Figure 4.6: Left: The conventional coordinate system of CMS with momentum vector \vec{p} . Taken from [37]. Right: Pseudorapidity. Taken from [38].

160 **4.2.1 Coordinate system**

161 The conventional coordinate system of CMS is defined in Fig. 4.6.

162 **4.2.2 The solenoid magnet & flux-return yoke**

163 The *superconducting solenoid magnet* is a 13 m long cylinder with an inner diameter of 6 m. The
164 yoke [42].

165 **4.2.3 The pixel tracker**

166 The inner tracker system has a *silicon pixel tracker* and a *silicon microstrip tracker*. Figure 4.8
167 presents a closer look of the full tracker layout. The pixel tracker from 2008 up to 2016 was
168 composed of 1440 sensor modules with a total of 66 million silicon pixels [43]. During the
169 technical shutdown it was upgraded with 1856 modules with 124 million pixels in total [41, 44].
170 Their layouts are compared in Fig. 4.9. See Refs. [43, 45] for more information on the resolution.

171 **4.2.4 The silicon strip tracker**

172 The silicon strip tracker is larger. A detailed description of the tracking and vertexing software
173 is given in Ref. [43].

174 **4.2.5 The electromagnetic calorimeter**

175 The *electromagnetic calorimeter* (ECAL) is built around the tracker. The energy resolution can
176 be parametrized as a function of energy [36]:

$$\left(\frac{\sigma_E}{E}\right)^2 = \left(\frac{S}{\sqrt{E}}\right)^2 \oplus \left(\frac{N}{E}\right)^2 \oplus C^2, \quad (4.3)$$

177 with the stochastic term S , the noise N , and a constant term C . The technical design report [46]
178 describes the ECAL in more technical detail.

179 **4.2.6 The hadronic calorimeter**

180 The last subdetector inside the solenoid is the *hadron calorimeter* (HCAL). The jet energy
181 resolution can be found in Ref. [47]

182 The *very forward HCAL* (HF) is positioned around the beamline outside the detector.

183 **4.2.7 The muon system**

184 The muon system is outside the solenoid magnet. The final momentum resolution can be roughly
185 parametrized as follows:

$$\left(\frac{\sigma_{p_T}}{p_T}\right)^2 = (A \cdot p_T)^2 \oplus C^2, \quad (4.4)$$

186 where A , and C are constants determined by the hit resolution and multiple scattering, respec-
187 tively [48]. The resolution grows with momentum, because the track becomes more straight,
188 which increases the uncertainty in its curvature. The technical design report can be found in
189 Ref. [49].

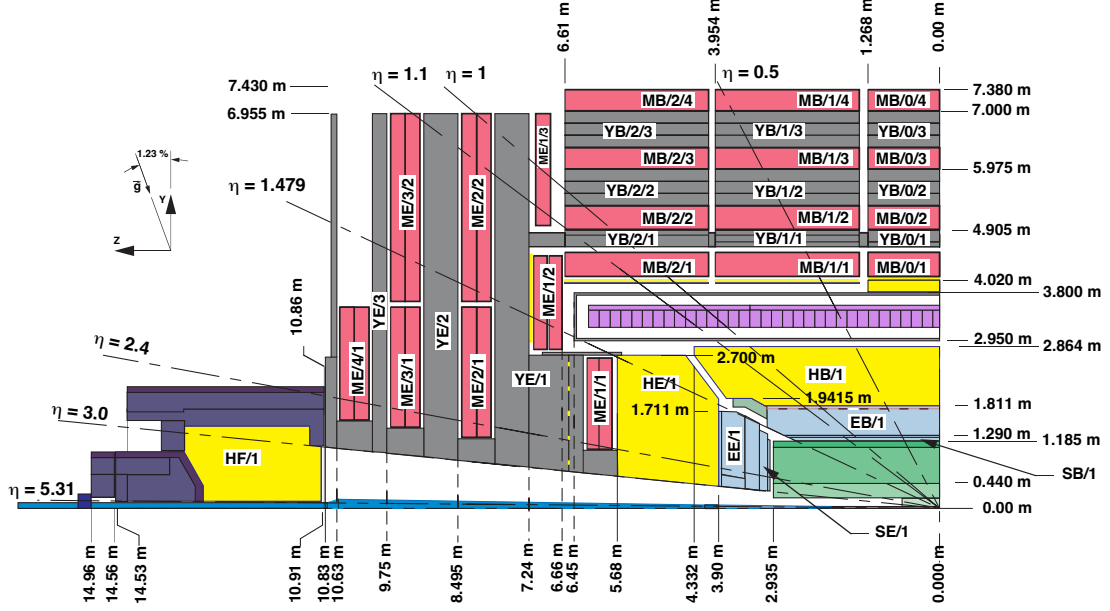


Figure 4.7: Schematic of one quadrant of the CMS detector in the positive zy -plane. Adapted from [39].

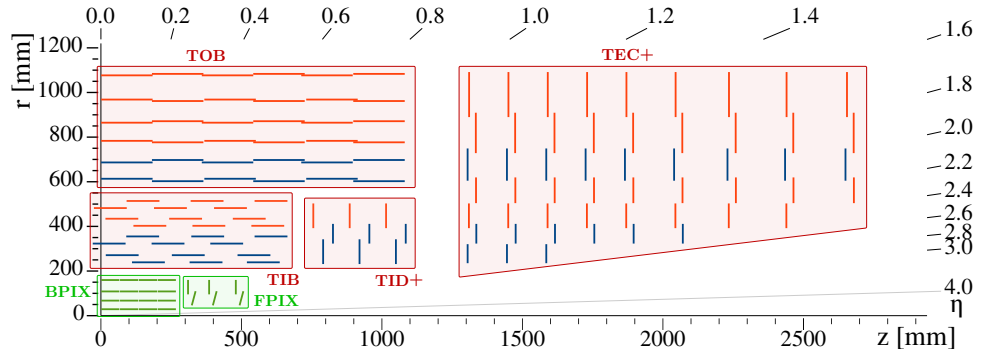


Figure 4.8: Schematic view of the CMS tracking system. Adapted from [40].

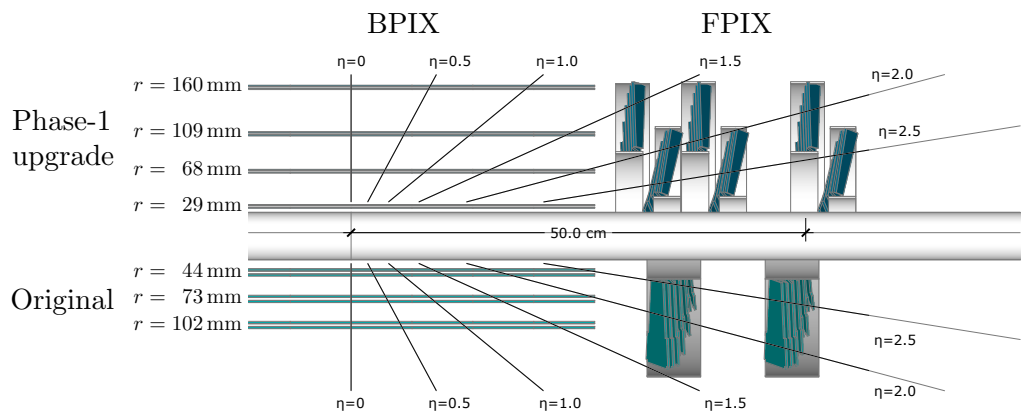


Figure 4.9: Layout of the CMS pixel detector. Adapted from [41].

190 **4.2.8 The trigger system**

191 The collision rate of 40 MHz is higher than is possible to record offline. The *L1 trigger* has a
192 rate of about 100 kHz. The next level, is the *high-level trigger* (HLT). See Ref. [50].

193 5 Object & Event Reconstruction

194 This chapter explains object and event reconstruction in the CMS experiment.

195 5.1 Principles of particle identification

196 Figure 5.1 compares the lifetime, dividing them in different regions of stability in the context of
197 the CMS experiment.

198 Each of these particles has a unique set of properties that leave a characteristic signal in one
199 or more of the subdetector, as illustrated in Fig. 5.2.

200 5.2 Particle-flow algorithm

201 The particle-flow (PF) algorithm [53, 54] fully reconstructs the event of a pp collision with an
202 optimized combination of all measurements of the CMS subsystems.

203 Tracks in the inner tracker or muon system are iteratively built from hits, using the *Kalman-*
204 *filter (KF) technique* [55, 56].

205 5.3 Primary vertex

206 The algorithm locates primary vertices (PVs) of pp collisions. The tracks are clustered using the
207 *deterministic annealing algorithm* [57]. Finally, candidate vertices are fitted using an *adaptive*
208 *vertex fitter* [58]. The PV with the largest sum of momenta is assumed to be the vertex of the
209 hard scattering process [43, 54, 59].

210 5.4 Electrons

211 Electrons are reconstructed by associating a track in the inner tracker to clusters of energy
212 deposits in the ECAL. Candidate tracks are refitted with the *Gaussian sum filter* (GSF) [60].
213 The ECAL clusters are recombined into a so-called *supercluster*. The resolution is documented
214 in Ref. [61, 62].

215 The reconstruction and identification of electrons, as well as high-energy photons, are dis-
216 cussed in more detail in Refs. [63] and [61].

217 The *relative isolation* for electrons is computed with the so-called *rho-effective-area method* [64]:

$$I_{\text{rel}}^e := \frac{\sum_{\text{charged}} p_T + \max(0, \sum_{\text{neutral}} E_T - \rho A_{\text{eff}})}{p_T^e}. \quad (5.1)$$

218 5.5 Muons

219 Muon candidates in CMS are reconstructed as *standalone muons*, *tracker muons*, and/or *global*
220 *muons* [65].

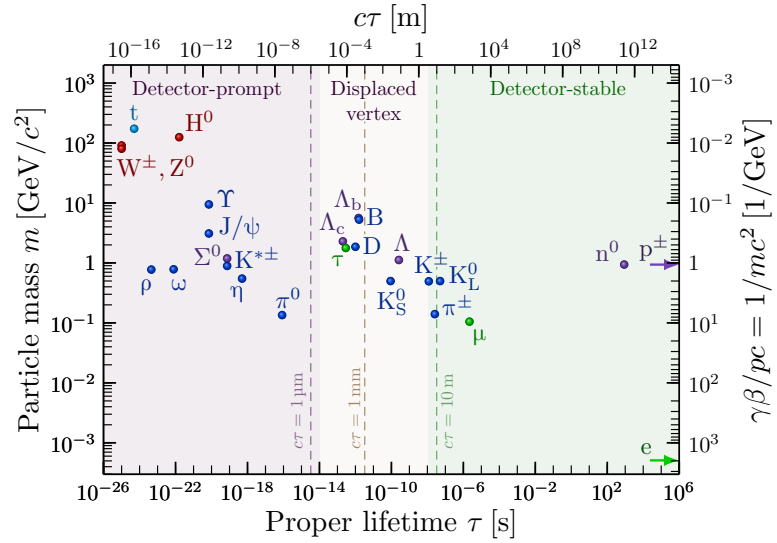


Figure 5.1: Plot of the mass versus lifetime τ of many composite and fundamental SM particles. The decay length is given by $L = \gamma\beta c\tau$, with $\gamma\beta = p/mc$. Adapted from [51].

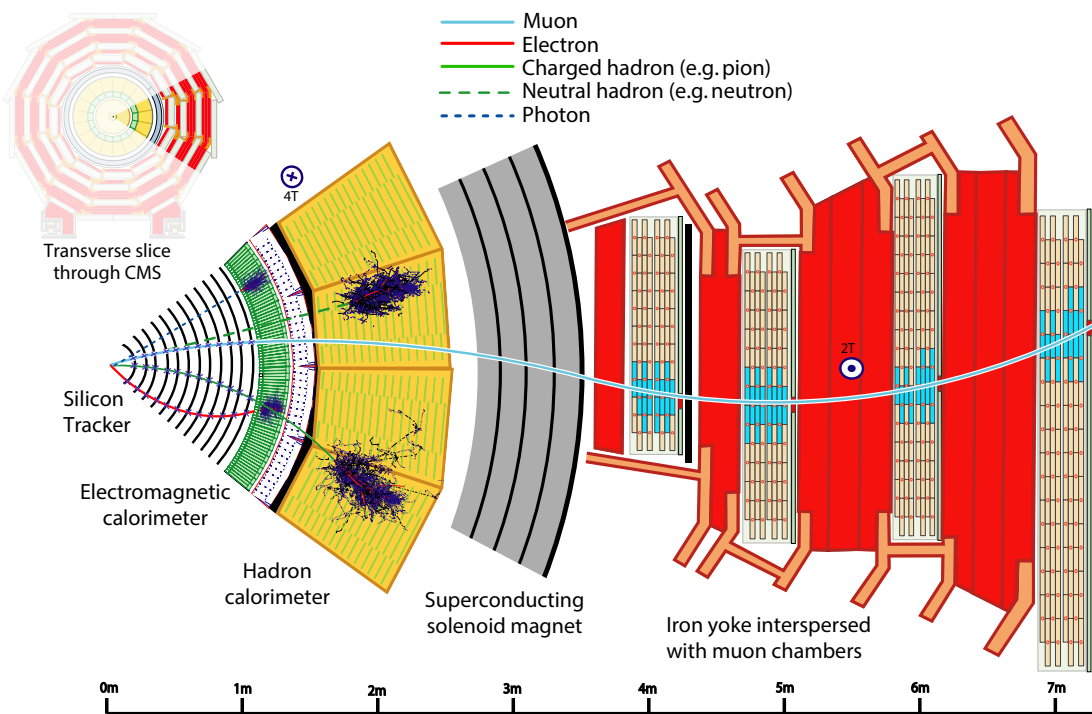


Figure 5.2: Particles in the CMS detector. Adapted from from [52].

221 The relative isolation of a muon is defined with the so-called $\Delta\beta$ -corrections:

$$I_{\text{rel}}^{\mu} := \frac{\sum_{\text{charged}} p_T + \max(0, \sum_{\text{neutral}} E_T - \Delta\beta \sum_{\text{charged, PU}} p_T)}{p_T^{\mu}}. \quad (5.2)$$

222 5.6 Hadronically Decayed τ Leptons

223 Hadronic decays of τ leptons (τ_h) are reconstructed with the *hadron-plus-strips* (HPS) algorithm
224 [66–69]. About 65% of hadronic τ decays involve neutral pions, which decay promptly ($\tau =$
225 8.4×10^{-17} s) to two photons 98.8% of the time [10, p. 33].

226 The τ_h identification algorithm DEEPTAU [69] was used to discriminate against jets that are
227 initiated by quarks and gluons, as well as electrons and muons, see Fig. 5.5.

228 5.7 Jets

229 Jets are reconstructed with a clustering algorithm. The jet properties must be *infrared safe* and
230 *collinear safe*. The *anti- k_T* (AK) algorithm utilizes the metric

$$d_{ij} = \min(p_{T,i}^{-2}, p_{T,j}^{-2}) \frac{\Delta R_{ij}^2}{\Delta R_y^2}, \quad (5.3)$$

231 where $\Delta R_y = \sqrt{\Delta y^2 + \Delta\phi^2}$ is the distance in (y, ϕ) -space with the *rapidity*

$$y := \frac{1}{2} \ln \left(\frac{E + p_z}{E - p_z} \right). \quad (5.4)$$

232 If a cluster i of combined objects satisfies

$$d_{ij} > d_{iB} = p_{T,i}^{-2}, \quad (5.5)$$

233 More info is given in Ref. [54, 71]. The AK algorithm is implemented in the FASTJET library [72,
234 73], and *charged-hadron subtraction* (CHS) is used.

235 The CMS Collaboration determines *jet energy corrections* (JECs) in several steps, which are
236 explained in detail in Ref. [74]. Additionally, the jet energy and *jet energy resolution* (JER) of
237 jets in simulation are corrected to obtain better agreement between simulation and data.

238 Genuine jets are distinguished from pileup jets with the identification algorithm [75]. Iden-
239 tification [76] removes spurious jet-like features that originate from isolated noise patterns in
240 certain HCAL regions.

241 5.8 Bottom quark identification

242 The DEEPCSV algorithm [77, 78] for b tagging jets. DEEPCSV is a deep neural network
243 (DNN) with four hidden layers that is an extension of the combined secondary vertex (CSV)
244 algorithm [77, 78].

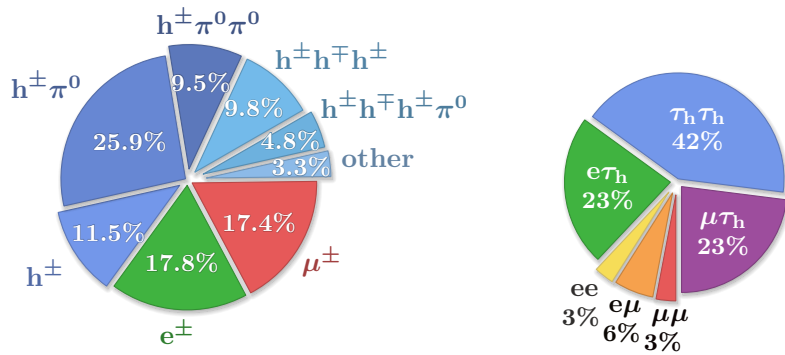


Figure 5.3: Pie charts of branching fractions. **Left:** τ lepton decay. **Right:** Decay channels of a pair of τ leptons. Numbers from PDG [10, p. 28].

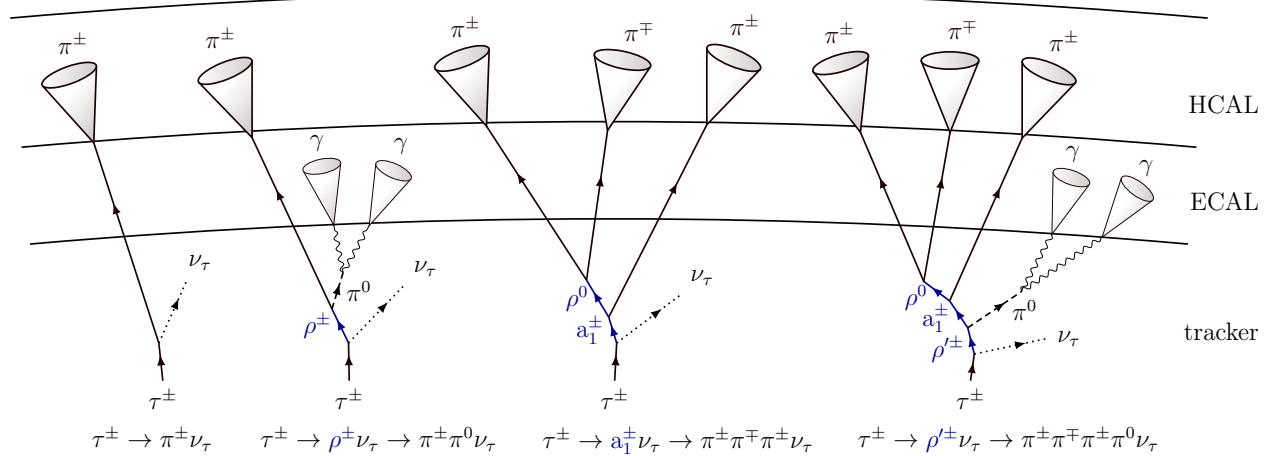


Figure 5.4: An illustration τ_h signatures. Inspired by Ref. [70, p. 37].

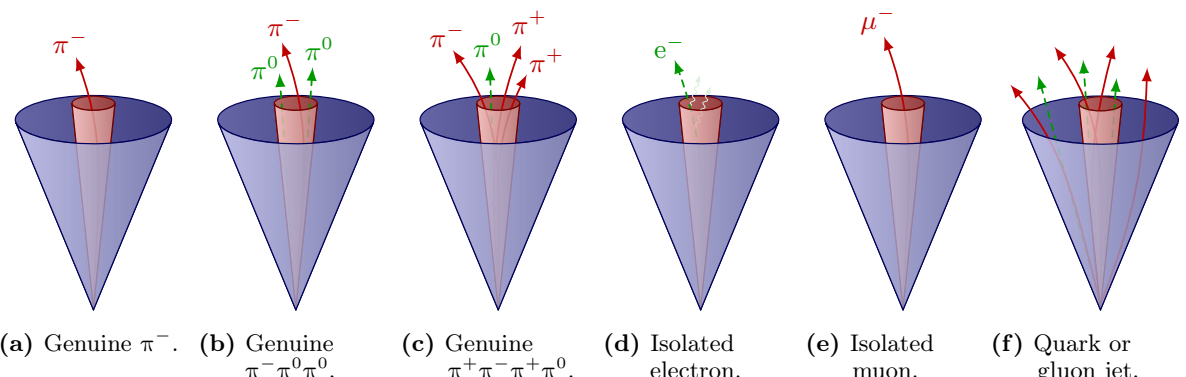


Figure 5.5: Illustration of several hadronic decay modes of the τ leptons (a-c) and their backgrounds (d-f).

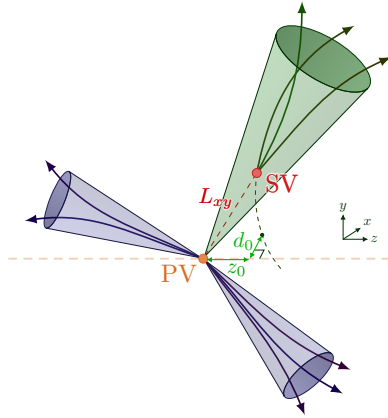


Figure 5.6: B-tagging.

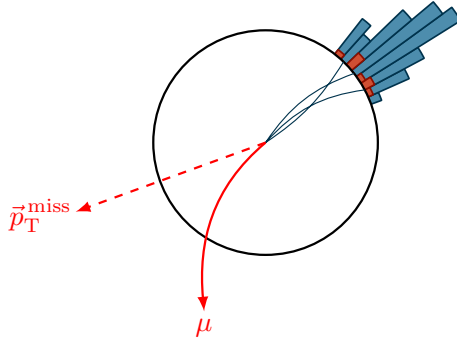


Figure 5.7: Illustration of missing transverse energy (MET) with a muon track (red), and energy deposits in the calorimeters.

245 **5.9 Missing transverse energy**

246 The vectorially sum of all particles gives the missing momentum

$$\vec{p}_T^{\text{miss}} = - \sum_i \vec{p}_T^i. \quad (5.6)$$

247 This vector, or its length, is often referred to as the *missing transverse momentum*, or *missing
248 transverse energy* (MET). Several corrections are applied [54]. More details can be found in
249 Refs. [79] and [80].

250 **6 Data sets & Simulated Samples**

251 This chapter will discuss in more detail the data sets of pp collision events used, as well as the
252 samples of simulated background events.

253 **6.1 Data sets**

254 The total data set recorded between 2016 and 2018 corresponds to an integrated luminosity of
255 approximately 138 fb^{-1} at $\sqrt{s} = 13 \text{ TeV}$. The run ranges and integrated luminosity per year are
256 listed in Table 6.1.

Table 6.1: LHC run number ranges and integrated luminosity L .

| Run number range | $L [\text{fb}^{-1}]$ |
|------------------|----------------------|
| 272007–284044 | 36.3 |
| 297020–306462 | 41.5 |
| 315252–325175 | 59.7 |

257 **6.2 Event simulation**

258 The PYTHIA parameters affecting the description of the underlying event are set to the CUETP8M1
259 (CP5) tune for all 2016 (2017 and 2018) samples [82, 83], except for the 2016 $t\bar{t}$ sample, for
260 which CUETP8M2T4 [84] is used. The interaction with the CMS detector is simulated by
261 GEANT4 [85]. Pileup is generated with PYTHIA. Event generation is described in more detail in
262 Refs. [10, p. 717], [86] and [87].

263 **6.3 Backgrounds**

264 **6.3.1 Simulated backgrounds**

265 All the simulated background samples used in this thesis are listed in Table 6.2. The $W + \text{jets}$ and
266 $Z + \text{jets}$ processes are generated with MADGRAPH [88] at LO precision. The MLM jet matching
267 and merging scheme [89] is used to match partons between MADGRAPH and PYTHIA and prevent
268 overcounting. The $Z + \text{jets}$ samples generated at NLO by MADGRAPH5_aMC@NLO [90]. The
269 production of $t\bar{t}$ and singly produced top quarks is simulated with the POWHEG [91–93] 2.0 and
270 1.0 generators, respectively, at NLO precision [94–97]. Diboson production is generated at LO
271 with PYTHIA 8 [98, 99]. The NNPDF3.0 PDF sets [100] are used for 2016. The NNPDF3.1
272 PDF [24] sets are used for 2017 and 2018 samples.

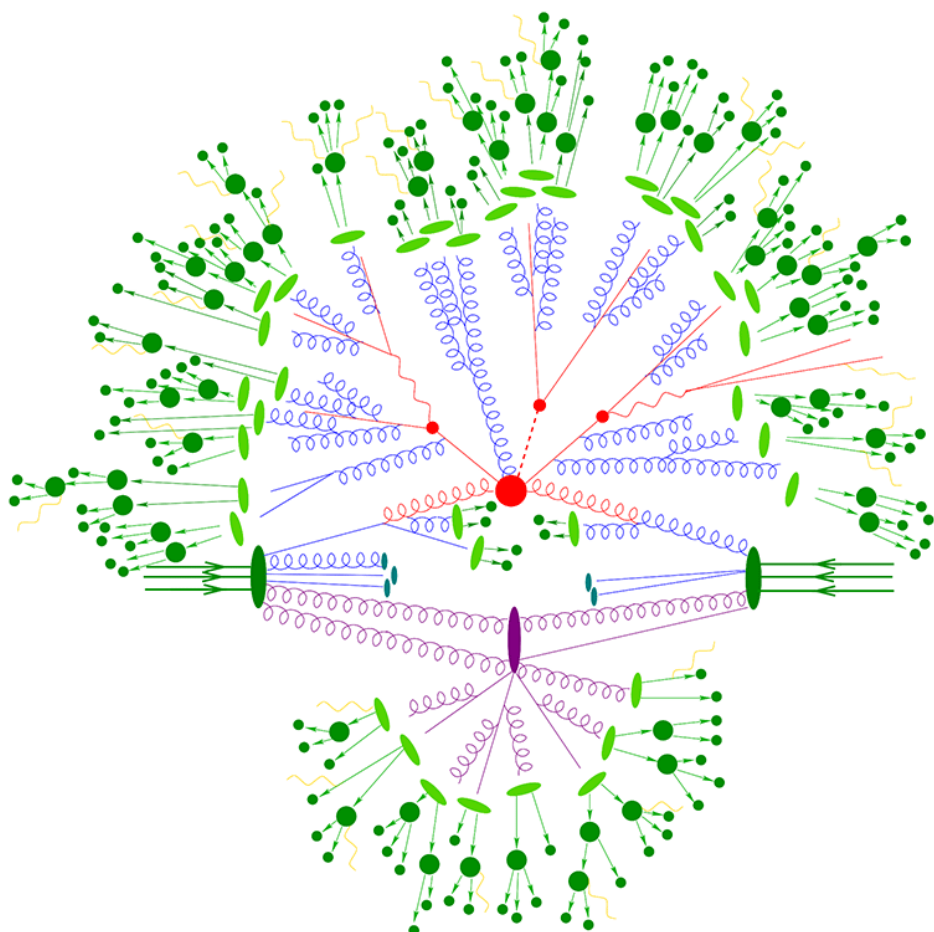


Figure 6.1: Schematic diagram explaining event generation of two colliding protons. Retrieved from [81].

Table 6.2: Summary of simulated SM backgrounds

| Process | Generators | Cross section σ [pb] |
|---|------------------|---------------------------------------|
| Drell-Yan, $Z/\gamma^* \rightarrow \ell^+\ell^-$, LO | | |
| + jets, $10 < m_{\ell\ell} < 50$ GeV | MADGRAPH, PYTHIA | 15810.0 (LO), 18610.0 (NLO) |
| + jets, $m_{\ell\ell} > 50$ GeV | MADGRAPH, PYTHIA | 5343.0 (LO), 6077.2 (NNLO) |
| + 1 jets, $m_{\ell\ell} > 50$ GeV | MADGRAPH, PYTHIA | 877.8 (LO) |
| + 2 jets, $m_{\ell\ell} > 50$ GeV | MADGRAPH, PYTHIA | 304.4 (LO) |
| + 3 jets, $m_{\ell\ell} > 50$ GeV | MADGRAPH, PYTHIA | 111.5 (LO) |
| + 4 jets, $m_{\ell\ell} > 50$ GeV | MADGRAPH, PYTHIA | 44.05 (LO) |
| Drell-Yan, $Z/\gamma^* \rightarrow \ell^+\ell^-$, NLO | | |
| + jets, $m_{\ell\ell} \in [100, 200]$ GeV | aMC@NLO, PYTHIA | 247.8 (NLO) |
| + jets, $m_{\ell\ell} \in [200, 400]$ GeV | aMC@NLO, PYTHIA | 8.502 (NLO) |
| + jets, $m_{\ell\ell} \in [400, 500]$ GeV | aMC@NLO, PYTHIA | 0.4514 (NLO) |
| + jets, $m_{\ell\ell} \in [500, 700]$ GeV | aMC@NLO, PYTHIA | 0.2558 (NLO) |
| + jets, $m_{\ell\ell} \in [700, 800]$ GeV | aMC@NLO, PYTHIA | 0.04023 (NLO) |
| + jets, $m_{\ell\ell} \in [800, 1000]$ GeV | aMC@NLO, PYTHIA | 0.03406 (NLO) |
| + jets, $m_{\ell\ell} \in [1000, 1500]$ GeV | aMC@NLO, PYTHIA | 0.01828 (NLO) |
| + jets, $m_{\ell\ell} \in [1500, 2000]$ GeV | aMC@NLO, PYTHIA | 0.002367 (NLO) |
| + jets, $m_{\ell\ell} \in [2000, 3000]$ GeV | aMC@NLO, PYTHIA | 5.409×10^{-4} (NLO) |
| + jets, $m_{\ell\ell} \in [3000, \infty]$ GeV | aMC@NLO, PYTHIA | 3.048×10^{-5} (NLO) |
| W + jets, $W \rightarrow \ell\nu$ | | |
| + jets | MADGRAPH, PYTHIA | 52940.0 (LO), 61526.7 (NLO) |
| + 1 jets | MADGRAPH, PYTHIA | 8104.0 (LO) |
| + 2 jets | MADGRAPH, PYTHIA | 2793.0 (LO) |
| + 3 jets | MADGRAPH, PYTHIA | 992.5 (LO) |
| + 4 jets | MADGRAPH, PYTHIA | 544.3 (LO) |
| t̄t + jets | | 833.9 (NNLO) |
| Fully leptonic | POWHEG, PYTHIA | 88.29 (NNLO), $\mathcal{B} = 10.6\%$ |
| Semi-leptonic | POWHEG, PYTHIA | 365.35 (NNLO), $\mathcal{B} = 43.9\%$ |
| Fully Hadronic | POWHEG, PYTHIA | 377.96 (NNLO), $\mathcal{B} = 45.4\%$ |
| Single top | | |
| t + W ⁻ | POWHEG, PYTHIA | 35.85 (NNLO) |
| ̄t + W ⁺ | POWHEG, PYTHIA | 35.85 (NNLO) |
| Single t, t channel | POWHEG, PYTHIA | 136.02 (NNLO) |
| Single ̄t, t channel | POWHEG, PYTHIA | 80.95 (NNLO) |
| Diboson | | |
| WW | PYTHIA | 75.88 (LO) |
| WZ | PYTHIA | 27.60 (LO) |
| ZZ | PYTHIA | 12.14 (LO) |

273 **6.3.2 Cross sections**

274 Table 6.2 also lists the theoretical cross sections σ for each sample. The events are weighted by

$$Z = \frac{L\sigma}{N_{\text{tot}}}, \quad (6.1)$$

275 or with generator weight w_{gen} ,

$$Z = \frac{L\sigma}{\sum w_{\text{gen}}} w_{\text{gen}}. \quad (6.2)$$

276 The LO cross sections of the Z + jets and W + jets samples in Table 6.2 are computed with
277 MADGRAPH. The Z + jets cross section is computed with FEWZ [101] program at NNLO in per-
278 turbative QCD, and with NLO electroweak corrections. The tt}+jets cross section was computed
279 with the TOP++v2.0 program [102, 103] at NNLO and at next-to-next-to-leading logarithmic
280 (NNLL) accuracy. The W + jets production is normalized with cross sections computed at NLO
281 accuracy.

7 Event Selection

This chapter will discuss in more detail the data sets of pp collision events used, as well as the samples of simulated background events.

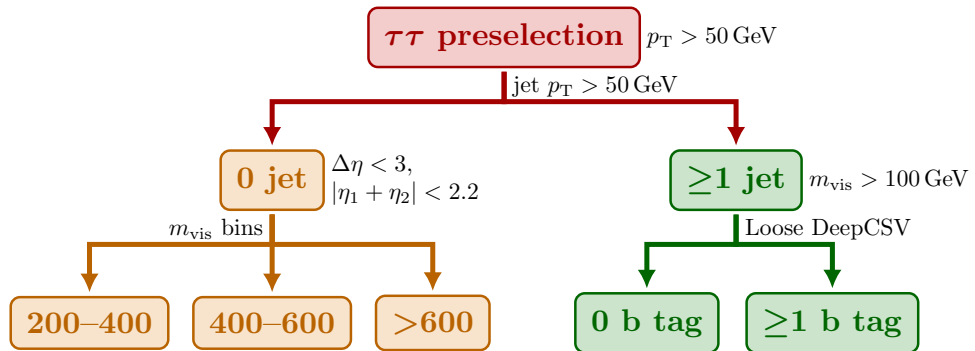


Figure 7.1: Flow chart of event selection.

285 References

- [1] CMS Collaboration, “Observation of a new boson at a mass of 125 GeV with the CMS experiment at the LHC”, *Phys. Lett. B* **716** (2012) 30,
doi:10.1016/j.physletb.2012.08.021, arXiv:1207.7235.
- [2] ATLAS Collaboration, “Observation of a new particle in the search for the Standard Model Higgs boson with the ATLAS detector at the LHC”, *Phys. Lett. B* **716** (2012) 1,
doi:10.1016/j.physletb.2012.08.020, arXiv:1207.7214.
- [3] CMS Collaboration, “Observation of a new boson with mass near 125 GeV in pp collisions at $\sqrt{s} = 7$ and 8 TeV”, *JHEP* **06** (2013) 081,
doi:10.1007/JHEP06(2013)081, arXiv:1303.4571.
- [4] F. Englert and R. Brout, “Broken Symmetry and the Mass of Gauge Vector Mesons”,
Phys. Rev. Lett. **13** (1964) 321, doi:10.1103/PhysRevLett.13.321.
- [5] P. W. Higgs, “Broken Symmetries and the Masses of Gauge Bosons”, *Phys. Rev. Lett.* **13** (1964) 508, doi:10.1103/PhysRevLett.13.508.
- [6] L. M. Brown, M. Dresden, L. H. Hoddeson, and M. West, eds., “Proceedings, 2nd International Symposium on on the History of Particle Physics in the 1950s: Pions to Quarks: Batavia, USA, May 1-4, 1985”. Univ. Pr., Cambridge, UK, (1989).
- [7] L. H. Hoddeson, L. Brown, M. Riordan, and M. Dresden, eds., “The Rise of the standard model: Particle physics in the 1960s and 1970s. Proceedings, Conference, Stanford, USA, June 24-27, 1992”. (1997).
- [8] D. Griffiths, “Introduction to Elementary Particles”. Wiley-VCH, 2 edition, 2008.
ISBN 978-3-527-40601-2.
- [9] Neutelings, Izaak, “History timeline and energy scales – TikZ.net”,
<https://tikz.net/timeline/>, 2022. (Retrieved March 26, 2022).
- [10] Particle Data Group, “Review of Particle Physics”, *PTEP* **2022** (2022) 083C01,
doi:10.1093/ptep/ptac097.
- [11] ATLAS and CMS Collaborations, “Combined Measurement of the Higgs Boson Mass in pp Collisions at $\sqrt{s} = 7$ and 8 TeV with the ATLAS and CMS Experiments”, *Phys. Rev. Lett.* **114** (2015) 114, doi:10.1103/PhysRevLett.114.191803, arXiv:1503.07589.
- [12] A. Ferrari and N. Rompotis, “Exploration of Extended Higgs Sectors with Run-2 Proton–Proton Collision Data at the LHC”, *Symmetry* **13** (2021), no. 11, 2144,
doi:10.3390/sym14081546. [Erratum: Symmetry 14, 1546 (2022)].
- [13] Wikimedia Commons, “File:Standard Model of Elementary Particles.svg — Wikimedia Commons, the free media repository”, https://commons.wikimedia.org/wiki/File:Standard_Model_of_Elementary_Particles.svg, 2023. (Retrieved Jan 13, 2023).
- [14] G. Isidori, “Lectures notes on Flavour physics”,

- 321 <https://www.physik.uzh.ch/en/groups/isidori/teaching.html>, 2016. (Retrieved
 322 Nov 16, 2022).
- 323 [15] S. L. Glashow, J. Iliopoulos, and L. Maiani, “Weak Interactions with Lepton-Hadron
 324 Symmetry”, *Phys. Rev. D* **2** (1970) 1285, doi:10.1103/PhysRevD.2.1285.
- 325 [16] E. D. Bloom et al., “High-Energy Inelastic e^-p Scattering at 6° and 10° ”, *Phys. Rev.*
 326 *Lett.* **23** (1969) 930, doi:10.1103/PhysRevLett.23.930.
- 327 [17] M. Breidenbach et al., “Observed Behavior of Highly Inelastic Electron-Proton
 328 Scattering”, *Phys. Rev. Lett.* **23** (1969) 935, doi:10.1103/PhysRevLett.23.935.
- 329 [18] **ZEUS** and **H1** Collaborations, “Combination of measurements of inclusive deep inelastic
 330 $e^\pm p$ scattering cross sections and QCD analysis of HERA data”, *Eur. Phys. J. C* **75**
 331 (2015), no. 12, 580, doi:10.1140/epjc/s10052-015-3710-4, arXiv:1506.06042.
- 332 [19] R. P. Feynman, “The Behavior of Hadron Collisions at Extreme Energies”, in *High*
 333 *Energy Collisions: Third International Conference*, p. 237. Stony Brook, N.Y., U.S.A.,
 334 1969.
- 335 [20] J. D. Bjorken and E. A. Paschos, “Inelastic Electron-Proton and γ -Proton Scattering and
 336 the Structure of the Nucleon”, *Phys. Rev.* **185** (1969) 1975,
 337 doi:10.1103/PhysRev.185.1975.
- 338 [21] J. M. Campbell, J. W. Huston, and W. J. Stirling, “Hard Interactions of Quarks and
 339 Gluons: A Primer for LHC Physics”, *Rept. Prog. Phys.* **70** (2007) 89,
 340 doi:10.1088/0034-4885/70/1/R02, arXiv:hep-ph/0611148.
- 341 [22] R. Placakyte, “Parton Distribution Functions”, in *Proceedings, 31st International*
 342 *Conference on Physics in collisions (PIC 2011)*. Vancouver, Canada, 2011.
 343 arXiv:1111.5452.
- 344 [23] **ALICE** Collaboration, “Parton distributions for the LHC”, *Eur. Phys. J. C* **63** (2009)
 345 189, doi:10.1140/epjc/s10052-009-1072-5, arXiv:0901.0002.
- 346 [24] **NNPDF** Collaboration, “Parton distributions from high-precision collider data”, *Eur.*
 347 *Phys. J. C* **77** (2017), no. 10, 663, doi:10.1140/epjc/s10052-017-5199-5,
 348 arXiv:1706.00428.
- 349 [25] J. C. Collins and D. E. Soper, “The Theorems of Perturbative QCD”, *Ann. Rev. Nucl.*
 350 *Part. Sci.* **37** (1987) 383, doi:10.1146/annurev.ns.37.120187.002123.
- 351 [26] J. C. Collins, D. E. Soper, and G. F. Sterman, “Factorization of Hard Processes in
 352 QCD”, *Adv. Ser. Direct. High Energy Phys.* **5** (1989) 11,
 353 doi:10.1142/9789814503266_0001, arXiv:hep-ph/0409313.
- 354 [27] T. Aoyama, M. Hayakawa, T. Kinoshita, and M. Nio, “Tenth-Order QED Contribution
 355 to the Electron g-2 and an Improved Value of the Fine Structure Constant”, *Phys. Rev.*
 356 *Lett.* **109** (2012) 111807, doi:10.1103/PhysRevLett.109.111807, arXiv:1205.5368.
- 357 [28] T. Aoyama, M. Hayakawa, T. Kinoshita, and M. Nio, “Tenth-Order Electron Anomalous
 358 Magnetic Moment — Contribution of Diagrams without Closed Lepton Loops”, *Phys.*
 359 *Rev. D* **91** (2015), no. 3, 033006,
 360 doi:10.1103/PhysRevD.91.033006, 10.1103/PhysRevD.96.019901, arXiv:1412.8284.
 361 [Erratum: *Phys. Rev. D* 96, no. 1, 019901 (2017)].

- 362 [29] M. Nio, “QED tenth-order contribution to the electron anomalous magnetic moment and
 363 a new value of the fine-structure constant”, Fundamental Constants Meeting, Eltville,
 364 Germany, 2015. <http://www.bipm.org/cc/CODATA-TGFC/Allowed/2015-02/Nio.pdf>.
- 365 [30] D. Hanneke, S. Fogwell, and G. Gabrielse, “New Measurement of the Electron Magnetic
 366 Moment and the Fine Structure Constant”, *Phys. Rev. Lett.* **100** (2008) 120801,
 367 [doi:10.1103/PhysRevLett.100.120801](https://doi.org/10.1103/PhysRevLett.100.120801), arXiv:0801.1134.
- 368 [31] L. Forthomme (Wikimedia Commons), “File:Cern-accelerator-complex.svg — Wikimedia
 369 Commons, the free media repository”,
 370 <https://commons.wikimedia.org/wiki/File:Cern-accelerator-complex.svg>, 2016.
 371 (Retrieved Jul 24, 2017).
- 372 [32] S. Holmes, R. S. Moore, and V. Shiltsev, “Overview of the Tevatron Collider Complex:
 373 Goals, Operations and Performance”, *JINST* **6** (2011) T08001,
 374 [doi:10.1088/1748-0221/6/08/T08001](https://doi.org/10.1088/1748-0221/6/08/T08001), arXiv:1106.0909.
- 375 [33] L. Evans and P. Bryant, “LHC Machine”, *JINST* **3** (2008), no. 08, S08001,
 376 [doi:10.1088/1748-0221/3/08/S08001](https://doi.org/10.1088/1748-0221/3/08/S08001).
- 377 [34] CMS Collaboration, “Public CMS Luminosity Information”.
 378 <https://twiki.cern.ch/twiki/bin/view/CMSPublic/LumiPublicResults>. (Retrieved
 379 Dec 6, 2022).
- 380 [35] I. Efthymiopoulos et al., “Bunch Luminosity Variations in LHC Run 2. BUNCH
 381 LUMINOSITY VARIATIONS IN LHC RUN 2”, *JACoW IPAC* **2021** (2021) 4094,
 382 [doi:10.18429/JACoW-IPAC2021-THPAB172](https://doi.org/10.18429/JACoW-IPAC2021-THPAB172).
- 383 [36] CMS Collaboration, “The CMS experiment at the CERN LHC”, *JINST* **3** (2008)
 384 S08004, [doi:10.1088/1748-0221/3/08/S08004](https://doi.org/10.1088/1748-0221/3/08/S08004).
- 385 [37] Neutelings, Izaak, “CMS coordinate system – TikZ.net”,
 386 https://tikz.net/axis3d_cms/, 2022. (Retrieved Dec 2, 2022).
- 387 [38] Neutelings, Izaak, “Pseudorapidity – TikZ.net”,
 388 https://tikz.net/axis2d_pseudorapidity/, 2022. (Retrieved Dec 2, 2022).
- 389 [39] CMS Collaboration, “Performance of the CMS Drift Tube Chambers with Cosmic Rays”,
 390 *JINST* **5** (2010) T03015, [doi:10.1088/1748-0221/5/03/T03015](https://doi.org/10.1088/1748-0221/5/03/T03015), arXiv:0911.4855.
- 391 [40] CMS Collaboration, “CMS Tracker Detector Performance Results”,
 392 <https://twiki.cern.ch/twiki/bin/view/CMSPublic/DPGResultsTRK>, 2022.
 393 (Retrieved Dec 2, 2022).
- 394 [41] CMS Tracker Group, “The CMS Phase-1 Pixel Detector Upgrade”, *JINST* **16** (2021),
 395 no. 02, P02027, [doi:10.1088/1748-0221/16/02/P02027](https://doi.org/10.1088/1748-0221/16/02/P02027), arXiv:2012.14304.
- 396 [42] CMS Collaboration, “Precise Mapping of the Magnetic Field in the CMS Barrel Yoke
 397 using Cosmic Rays”, *JINST* **5** (2015) T03021, [doi:10.1088/1748-0221/5/03/T03021](https://doi.org/10.1088/1748-0221/5/03/T03021),
 398 arXiv:0910.5530.
- 399 [43] CMS Collaboration, “Description and performance of track and primary-vertex
 400 reconstruction with the CMS tracker”, *JINST* **9** (2014) P10009,
 401 [doi:10.1088/1748-0221/9/10/P10009](https://doi.org/10.1088/1748-0221/9/10/P10009), arXiv:1405.6569.

- 402 [44] **CMS** Collaboration, “The Phase-1 upgrade of the CMS pixel detector”, *JINST* **12**
 403 (2017), no. 07, C07009, doi:10.1088/1748-0221/12/07/C07009.
- 404 [45] **CMS** Collaboration, “CMS Tracking POG Performance Plots For 2017 with PhaseI
 405 pixel detector”, [https://twiki.cern.ch/twiki/bin/view/CMSPublic/
 406 TrackingPOGPerformance2017MC#Vertex_Resolutions](https://twiki.cern.ch/twiki/bin/view/CMSPublic/TrackingPOGPerformance2017MC#Vertex_Resolutions), 2022. (Retrieved Dec 8, 2022).
- 407 [46] **CMS** Collaboration, “The CMS electromagnetic calorimeter project: Technical Design
 408 Report”, Technical Design Report CMS. CERN, Geneva, 1997.
- 409 [47] **CMS** Collaboration, “Jet energy scale and resolution in the CMS experiment in pp
 410 collisions at 8 TeV”, *JINST* **12** (2017), no. 02, P02014,
 411 doi:10.1088/1748-0221/12/02/P02014, arXiv:1607.03663.
- 412 [48] E. Manca, “Validation of the muon momentum resolution in view of the W mass
 413 measurement with the CMS experiment”. PhD thesis, INFN, Pisa, 2016.
 414 CMS-TS-2016-024, CERN-THESIS-2016-173.
- 415 [49] **CMS** Collaboration, “The CMS muon project : Technical Design Report”, Technical
 416 Design Report CMS. CERN, Geneva, 1997.
- 417 [50] **CMS** Collaboration, “The CMS trigger system”, *JINST* **12** (2017) P01020,
 418 doi:10.1088/1748-0221/12/01/P01020, arXiv:1609.02366.
- 419 [51] L. Lee, C. Ohm, A. Soffer, and T.-T. Yu, “Collider Searches for Long-Lived Particles
 420 Beyond the Standard Model”, *Prog. Part. Nucl. Phys.* **106** (2019) 210,
 421 doi:10.1016/j.ppnp.2019.02.006, arXiv:1810.12602. [Erratum:
 422 Prog.Part.Nucl.Phys. 122, 103912 (2022)].
- 423 [52] D. Barney, “CMS Slice”, <https://cds.cern.ch/record/2628641/>, 2015. (Retrieved
 424 Dec 8, 2022).
- 425 [53] **CMS** Collaboration, “Commissioning of the Particle-flow Event Reconstruction with the
 426 first LHC collisions recorded in the CMS detector”, CMS Physics Analysis Summary
 427 CMS-PAS-PFT-10-001, CERN, 2010.
- 428 [54] **CMS** Collaboration, “Particle-flow reconstruction and global event description with the
 429 CMS detector”, *JINST* **12** (2017) P10003, doi:10.1088/1748-0221/12/10/P10003,
 430 arXiv:1706.04965.
- 431 [55] W. Adam, B. Mangano, T. Speer, and T. Todorov, “Track Reconstruction in the CMS
 432 tracker”, technical report, CERN, Geneva, 2006.
- 433 [56] R. Frühwirth, “Application of Kalman filtering to track and vertex fitting”, *Nucl.
 434 Instrum. Meth. A* **262** (1987) 444, doi:10.1016/0168-9002(87)90887-4.
- 435 [57] K. Rose, “Deterministic annealing for clustering, compression, classification, regression,
 436 and related optimization problems”, *IEEE Proc.* **86** (1998), no. 11, 2210,
 437 doi:10.1109/5.726788.
- 438 [58] R. Frühwirth, W. Waltenberger, and P. Vanlaer, “Adaptive Vertex Fitting”, technical
 439 report, CERN, Geneva, 2007.
- 440 [59] **CMS** Collaboration, “Technical proposal for the Phase-II upgrade of the Compact Muon
 441 Solenoid”, CMS Technical Proposal CERN-LHCC-2015-010, CMS-TDR-15-02, CERN,

- 442 2015.
- 443 [60] W. Adam, R. Fröhwirth, A. Strandlie, and T. Todorov, “Reconstruction of electrons with
444 the Gaussian-sum filter in the CMS tracker at the LHC”, *Journal of Physics G: Nuclear
445 and Particle Physics* **31** (2005), no. 9, N9, doi:10.1088/0954-3899/31/9/n01.
- 446 [61] **CMS** Collaboration, “Electron and photon reconstruction and identification with the
447 CMS experiment at the CERN LHC”, *JINST* **16** (2021) P05014,
448 doi:10.1088/1748-0221/16/05/P05014, arXiv:2012.06888.
- 449 [62] **CMS** Collaboration, “ECAL 2016 refined calibration and Run2 summary plots”, CMS
450 Detector Performance Summary CMS-DP-2020-021, CERN, 2020.
- 451 [63] **CMS** Collaboration, “Performance of electron reconstruction and selection with the
452 CMS detector in proton-proton collisions at $\sqrt{s} = 8$ TeV”, *JINST* **10** (2015) P06005,
453 doi:10.1088/1748-0221/10/06/P06005, arXiv:1502.02701.
- 454 [64] M. Cacciari and G. P. Salam, “Pileup subtraction using jet areas”, *Phys. Lett. B* **659**
455 (2008) 119, doi:10.1016/j.physletb.2007.09.077, arXiv:0707.1378.
- 456 [65] **CMS** Collaboration, “Performance of the CMS muon detector and muon reconstruction
457 with proton-proton collisions at $\sqrt{s} = 13$ TeV”, *JINST* **13** (2018) P06015,
458 doi:10.1088/1748-0221/13/06/P06015, arXiv:1804.04528.
- 459 [66] **CMS** Collaboration, “Performance of τ -lepton reconstruction and identification in
460 CMS”, *JINST* **7** (2012), no. 01, P01001, doi:10.1088/1748-0221/7/01/P01001,
461 arXiv:1109.6034.
- 462 [67] **CMS** Collaboration, “Performance of reconstruction and identification of τ leptons
463 decaying to hadrons and ν_τ in pp collisions at $\sqrt{s} = 13$ TeV”, *JINST* **13** (2018) P10005,
464 doi:10.1088/1748-0221/13/10/P10005, arXiv:1809.02816.
- 465 [68] **CMS** Collaboration, “Performance of reconstruction and identification of tau leptons in
466 their decays to hadrons and tau neutrino in LHC Run-2”, CMS Physics Analysis
467 Summary CMS-PAS-TAU-16-002, CERN, 2016.
- 468 [69] **CMS** Collaboration, “Identification of hadronic tau lepton decays using a deep neural
469 network”, *JINST* **17** (2022), no. 07, P07023, doi:10.1088/1748-0221/17/07/p07023,
470 arXiv:2201.08458.
- 471 [70] Y. Takahashi and M. Tomoto, “Measurement of the top-quark pair production
472 cross-section in pp collisions at $\sqrt{s} = 7$ TeV using final states with an electron or a muon
473 and a hadronically decaying τ -lepton”. PhD thesis, Nagoya University, 2012.
474 CERN-THESIS-2012-252.
- 475 [71] M. Cacciari, G. P. Salam, and G. Soyez, “The anti- k_t jet clustering algorithm”, *JHEP*
476 **04** (2008) 063, doi:10.1088/1126-6708/2008/04/063, arXiv:0802.1189.
- 477 [72] M. Cacciari and G. P. Salam, “Dispelling the N^3 myth for the k_T jet-finder”, *Phys. Lett.*
478 *B* **641** (2006) 57, doi:10.1016/j.physletb.2006.08.037, arXiv:hep-ph/0512210.
- 479 [73] M. Cacciari, G. P. Salam, and G. Soyez, “FastJet user manual”, *Eur. Phys. J. C* **72**
480 (2012) 1896, doi:10.1140/epjc/s10052-012-1896-2, arXiv:1111.6097.
- 481 [74] **CMS** Collaboration, “Determination of jet energy calibration and transverse momentum

- resolution in CMS”, *JINST* **6** (2011) P11002, doi:10.1088/1748-0221/6/11/P11002, arXiv:1107.4277.
- [75] CMS Collaboration, “Pileup Jet Identification”, CMS Physics Analysis Summary CMS-PAS-JME-13-005, CERN, 2013.
- [76] CMS Collaboration, “Jet algorithms performance in 13 TeV data”, CMS Physics Analysis Summary CMS-PAS-JME-16-003, CERN, 2017.
- [77] D. Guest et al., “Jet Flavor Classification in High-Energy Physics with Deep Neural Networks”, *Phys. Rev. D* **94** (2016), no. 11, 112002, doi:10.1103/PhysRevD.94.112002, arXiv:1607.08633.
- [78] CMS Collaboration, “Identification of heavy-flavour jets with the CMS detector in pp collisions at 13 TeV”, *JINST* **13** (2018), no. 05, P05011, doi:10.1088/1748-0221/13/05/P05011, arXiv:1712.07158.
- [79] CMS Collaboration, “Performance of missing energy reconstruction in 13 TeV pp collision data using the CMS detector”, CMS Physics Analysis Summary CMS-PAS-JME-16-004, CERN, 2016.
- [80] CMS Collaboration, “Performance of missing transverse momentum in pp collisions at $\sqrt{s} = 13$ TeV using the CMS detector”, CMS Physics Analysis Summary CMS-PAS-JME-17-001, CERN, 2018.
- [81] SLAC Collaboration, “Simulations”.
<https://theory.slac.stanford.edu/our-research/simulations>. (Retrieved Jul 25, 2017).
- [82] CMS Collaboration, “Event generator tunes obtained from underlying event and multiparton scattering measurements”, *Eur. Phys. J. C* **76** (2016) 155, doi:10.1140/epjc/s10052-016-3988-x, arXiv:1512.00815.
- [83] CMS Collaboration, “Extraction and validation of a new set of CMS PYTHIA8 tunes from underlying-event measurements”, *Eur. Phys. J. C* **80** (2020) 4, doi:10.1140/epjc/s10052-019-7499-4, arXiv:1903.12179.
- [84] CMS Collaboration, “Investigations of the impact of the parton shower tuning in Pythia 8 in the modelling of $t\bar{t}$ at $\sqrt{s} = 8$ and 13 TeV”, CMS Physics Analysis Summary CMS-PAS-TOP-16-021, CERN, 2016.
- [85] GEANT4 Collaboration, “GEANT4 — a simulation toolkit”, *Nucl. Instrum. Meth. A* **506** (2003) 250, doi:10.1016/S0168-9002(03)01368-8.
- [86] M. H. Seymour and M. Marx, “Monte Carlo Event Generators”, in *Proceedings, 69th Scottish Universities Summer School in Physics: LHC Phenomenology (SUSSP69) 2012*, p. 287. St.Andrews, Scotland, U.K., 2013. arXiv:1304.6677. doi:10.1007/978-3-319-05362-2_8.
- [87] T. Sjöstrand, S. Mrenna, and P. Z. Skands, “PYTHIA 6.4 Physics and Manual”, *JHEP* **05** (2006) 026, doi:10.1088/1126-6708/2006/05/026, arXiv:hep-ph/0603175.
- [88] F. Maltoni and T. Stelzer, “MadEvent: Automatic event generation with MadGraph”, *JHEP* **02** (2003) 027, doi:10.1088/1126-6708/2003/02/027, arXiv:hep-ph/0208156.

- 522 [89] J. Alwall et al., “Comparative study of various algorithms for the merging of parton
 523 showers and matrix elements in hadronic collisions”, *Eur. Phys. J. C* **53** (2008) 473,
 524 doi:10.1140/epjc/s10052-007-0490-5, arXiv:0706.2569.
- 525 [90] J. Alwall et al., “The automated computation of tree-level and next-to-leading order
 526 differential cross sections, and their matching to parton shower simulations”, *JHEP* **07**
 527 (2014) 079, doi:10.1007/JHEP07(2014)079, arXiv:1405.0301.
- 528 [91] P. Nason, “A new method for combining NLO QCD with shower Monte Carlo
 529 algorithms”, *JHEP* **11** (2004) 040, doi:10.1088/1126-6708/2004/11/040,
 530 arXiv:hep-ph/0409146.
- 531 [92] S. Frixione, P. Nason, and C. Oleari, “Matching NLO QCD computations with parton
 532 shower simulations: the POWHEG method”, *JHEP* **11** (2007) 070,
 533 doi:10.1088/1126-6708/2007/11/070, arXiv:0709.2092.
- 534 [93] S. Alioli, P. Nason, C. Oleari, and E. Re, “A general framework for implementing NLO
 535 calculations in shower Monte Carlo programs: the POWHEG BOX”, *JHEP* **06** (2010)
 536 043, doi:10.1007/JHEP06(2010)043, arXiv:1002.2581.
- 537 [94] S. Frixione, P. Nason, and G. Ridolfi, “A positive-weight next-to-leading-order Monte
 538 Carlo for heavy flavour hadroproduction”, *JHEP* **09** (2007) 126,
 539 doi:10.1088/1126-6708/2007/09/126, arXiv:0707.3088.
- 540 [95] J. M. Campbell, R. K. Ellis, P. Nason, and E. Re, “Top-Pair Production and Decay at
 541 NLO Matched with Parton Showers”, *JHEP* **04** (2015) 114,
 542 doi:10.1007/JHEP04(2015)114, arXiv:1412.1828.
- 543 [96] S. Alioli, P. Nason, C. Oleari, and E. Re, “NLO single-top production matched with
 544 shower in POWHEG: s - and t -channel contributions”, *JHEP* **09** (2009) 111,
 545 doi:10.1088/1126-6708/2009/09/111, arXiv:0907.4076. [Erratum:
 546 doi:10.1007/JHEP02(2010)011].
- 547 [97] E. Re, “Single-top Wt-channel production matched with parton showers using the
 548 POWHEG method”, *Eur. Phys. J. C* **71** (2011) 1547,
 549 doi:10.1140/epjc/s10052-011-1547-z, arXiv:1009.2450.
- 550 [98] T. Sjöstrand, S. Mrenna, and Z. S., Peter, “A Brief Introduction to PYTHIA 8.1”,
 551 *Comput. Phys. Commun.* **178** (2008) 852, doi:10.1016/j.cpc.2008.01.036,
 552 arXiv:0710.3820.
- 553 [99] T. Sjöstrand et al., “An introduction to PYTHIA 8.2”, *Comput. Phys. Commun.* **191**
 554 (2015) 159, doi:10.1016/j.cpc.2015.01.024, arXiv:1410.3012.
- 555 [100] R. D. Ball et al., “Parton distributions for the LHC Run II”, *JHEP* **15** (2015) 40,
 556 doi:10.1007/JHEP04(2015)040, arXiv:1410.8849.
- 557 [101] K. Melnikov and F. Petriello, “Electroweak gauge boson production at hadron colliders
 558 through $O(\alpha(s)^{**2})$ ”, *Phys.Rev. D* **74** (2006) 114017,
 559 doi:10.1103/PhysRevD.74.114017, arXiv:hep-ph/0609070.
- 560 [102] M. Czakon and A. Mitov, “Top++: A Program for the Calculation of the Top-Pair
 561 Cross-Section at Hadron Colliders”, *Comput. Phys. Commun.* **185** (2014) 2930,
 562 doi:10.1016/j.cpc.2014.06.021, arXiv:1112.5675.

563 [103] “NNLO+NNLL top-quark-pair cross sections – ATLAS-CMS recommended predictions
564 for top-quark-pair cross sections using the Top++v2.0 program (M. Czakon, A. Mitov,
565 2013)”, <https://twiki.cern.ch/twiki/bin/view/LHCPhysics/TtbarNNLO>, 2022.
566 (Retrieved Dec 21, 2020).